Protection and Control of Modern Power Systems

ORIGINAL RESEARCH

Open Access

Grounding fault location method of overhead line based on dual-axis magnetic field trajectory

Xiaowei Wang[1*], Huan Du[1], Jie Gao[2], Xiangxiang Wei[3], Zhenfeng Liang[1], Liang Guo[4] and Weibo Liu[1]

Abstract

To address the challenges in fault location in distribution networks, the distribution of magnetic field under overhead line and its relationship with three-phase currents are explored in this paper. At the same time, considering the influence of sensor installation position, line sag and galloping on magnetic field, a grounding fault location method of an overhead line based on dual-axis magnetic field trajectory is proposed. The analytical expressions of the magnetic field on the *x*-axis and *y*-axis under the overhead line are obtained by least squares fitting. The Lissajous figure synthesized by dual-axis is then compared with the general equation of an ellipse, and the characteristic quantity expression characterizing the magnetic field trajectory structure is obtained. Finally, a fault location criterion is constructed using the difference of the characteristic quantities of the ellipses synthesized by *x*-axis and *y*-axis magnetic fields upstream and downstream of the fault point, i.e., the difference of the length of the major axis and the minor axis, and the sign for the ratio of the cosine value of the inclination angle. Compared with other location methods based on electrical quantity, the principle of this method is simpler and it can locate faults more quickly and accurately. A large number of simulation results show that the proposed method is suitable for different types of fault conditions.

Keywords Magnetic field, Fault location, Lissajous figure, Distribution network

1 Introduction

The safe and stable operation of a distribution network is the key factor in ensuring residents' reliable power supply and consumption. Fast and accurate fault location can help operators repair faults in a short time, so as to reduce power outage time and avoid economic losses. It is thus of great significance for the stable operation of the power grid and economic development.

At present, there is a lot of mature research on the fault location of high-voltage transmission lines. However, there are problems in the location methods proposed for a distribution network with a weak fault signal, and consequently, there is still a lack of adequate and reliable solutions [1, 2]. The location accuracy of the traditional impedance method [3–5] is easily affected by line parameters, grounding impedance and distributed generator connection. The application of traveling wave methods requires expensive devices, and therefore large investment. It is thus often used in high-voltage transmission lines and cables [6–8], while it is not suitable for distribution networks with many branches. Emerging artificial intelligence technologies such as ANN (Artificial neural network) [9] and K-NN (K-nearest neighbor) [10] need to train on a large amount of data and take a long time to process.

*Correspondence:
Xiaowei Wang
proceedings@126.com
[1] School of Electrical Engineering, Xi'an University of Technology, Xi'an 710048, China
[2] School of Electrical Engineering, Xi'an Jiaotong University, Xi'an, China
[3] Technische Universität Berlin, 10623 Berlin, Germany
[4] Jiangxi Electric Power Research Institute of State Grid, Nanchang 330000, China

In recent years, the non-contact location method based on electric and magnetic fields under overhead lines has become a research hotspot. Reference [11] discusses the case of replacing current transformers with magnetic field sensors as line monitoring devices, and proposes a combined algorithm based on the magnetic field to locate faults. As the basic elements of the magnetic field, the magnitude and direction can also be used as the basis of section location [12, 13], and the obtained magnetic field data can be further used to identify the fault type and determine the precise location of the fault. Reference [14] reconstructs the current through the magnetic field sensors, and combines the obtained current and magnetic field and fault characteristics to locate faults. This is suitable for multi-circuit transmission line. In [15], magnetic field sensors are only installed at individual locations (such as line terminals, substations portals, etc.), and traveling wave theory and Extended Kalman filter are combined to locate faults. This method does not use the low-cost advantage of magnetic field sensors, and the accuracy of the results is limited by the sampling rate of the device. In some studies, the electric field of the overhead line is also obtained by non-contact measurement, and the localization is achieved by the difference of the electric fields upstream and downstream of the fault point [16]. In fault detection, especially in the field of high impedance fault detection, the magnetic field-based methods still have good results. In [17], by introducing mathematical changes, the steady-state symmetrical component of the rotating magnetic field signal is obtained, as such processing can eliminate the influence of pole geometry. For high impedance faults involving tree branches, reference [18] uses giant magneto-resistive (GMR) to detect fault characteristics in the early stages of faults, whereas [19] extracts the transient characteristics of the magnetic signal through a multiresolution morphological gradient and classifies them with support vector machines. This method can distinguish high impedance faults from other transients, such as load switching, no-load transformer switching etc. In [20], the magnetic signal is decomposed by wavelet transform, and the fault detection and classification are realized by combining with a variance spectrum evaluation.

A method based on two-dimensional and three-dimensional ellipse trajectory analysis is widely used in power grid fault location, fault detection and power quality analysis. Reference [21] analyzes the three-dimensional polarization ellipse composed of three-phase voltages, and constructs the location criterion through the parametric equation of five ellipse parameters. In [22], three methods are proposed to realize the time domain protection of transmission lines based on the current and voltage characteristics in three-dimensional cartesian coordinates. The nonlinear voltage-current characteristic profile corresponding to the current and voltage waveforms can also be used as the basis for identifying high impedance faults [23]. In [24], the dynamic trajectories of the volt-ampere characteristics of the zero-sequence current and voltage in the characteristic frequency band are analyzed, and the high impedance fault is detected by the positive and negative sum of local rotation angles between two continuous vectors. Reference [25] quickly detects faults by judging whether the short sequence of points are inside the two-dimensional elliptical structure formed by voltage and current at normal operating conditions, while [26] uses three-phase voltage to synthesize rotation vector, and characterizes and classifies voltage sags and swells based on the elliptical parameter of rotation vector. References [27, 28] perform a Clarke transformation on the three-phase voltage, and a voltage sag parameter calculation and fault classification based on the transformed voltage ellipse.

In this paper, the sine function expressions of the x-axis and y-axis magnetic fields are obtained by least squares fitting, and the difference of characteristic quantities between the dual-axis magnetic field synthetic trajectories upstream and downstream of the fault point is analyzed. At the same time, considering the influence of the installation position of the sensor, line operation condition and data window, a distribution network grounding fault location method based on the characteristic quantities of elliptical trajectories of the magnetic field is proposed. Because the magnetic field sensors have many advantages such as low cost, easy installation and maintenance etc., more monitoring points can be installed to obtain sufficient line operating status information, so that the method has high accuracy and can realize accurate positioning of a distribution network. The number of sensors is determined based on three principles: importance of feeders; economy of power grid; and cooperation with the installed line monitoring device.

The main contributions of this paper are as follows:

1. By combining the sine function of the x-axis and y-axis magnetic fields fitted by the least squares method with the Lissajous figure, the two-dimensional figure is used to characterize the operational state of the line, thereby making full use of the magnetic field information in the direction of strong components (the z-axis component is weak and can be ignored).
2. Taking the three structural features (major axis, minor axis and inclination angle) of the Lissajous figure as the basis for fault location, the final results are

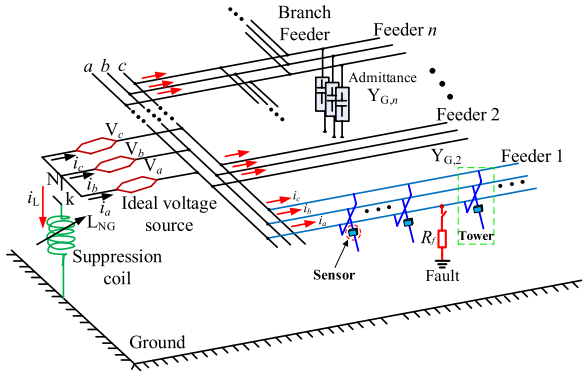

Fig. 1 Grounding fault model of distribution network

obtained by voting. This improves the reliability of fault location.

2 Theory analysis

2.1 Fault analysis

The power grid topology is shown in Fig. 1. It shows an A-phase grounding fault in a 10 kV distribution network. When the line operates normally, the current flowing through the phase conductor is:

$$I = I_C + I_L = j\omega C(E + U_0) + I_L \tag{1}$$

where I is the phase current, I_C is the phase to ground capacitance current, I_L is the load current of each phase, C is the phase to ground capacitance of the corresponding section, E is the power supply phase voltage, U_0 is the neutral point to ground voltage, and I_f is the fault current.

In the case of a fault, the fault phase currents upstream and downstream of the fault point of the fault feeder are given respectively as:

$$I'_a = I'_{aC} + I'_{aL} + I_f = j\omega C'(E_a + U') + I'_{aL} + I_f \tag{2}$$

$$I''_a = I'_{aC} + I'_{aL} = j\omega C''(E_a + U') + I'_{aL} \tag{3}$$

The healthy phase currents of the fault feeder are:

$$I'_b = I'_{bC} + I'_{bL} = j\omega C_b(E_b + U') + I'_{bL} \tag{4}$$

$$I'_c = I'_{cC} + I'_{cL} = j\omega C_c(E_c + U') + I'_{cL} \tag{5}$$

It can be seen that since the load current remains unchanged, the current change comes from the capacitance current generated by the line capacitance after the voltage change. The current variations of the two healthy phases of the fault feeder are basically the same, and are significantly less than the sudden change of the fault phase current upstream of the fault point. The current change of the downstream fault phase of the fault point has the same characteristics as those of the healthy phases, but is still much smaller than that of the upstream fault phase. Figure 2 shows the magnetic field distribution of the magnetic field sensor at different positions under the phase conductor.

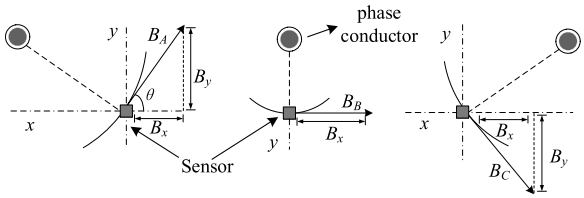

Fig. 2 Magnetic field distribution at the sensor

As shown in Fig. 2, the geometric relationship between the sensor and the phase conductor can be divided into three types. When the sensor is directly below the conductor, only the x-axis magnetic field is generated. When the conductor is obliquely below, the magnetic field generated by the current-carrying conductor can be divided into the x-axis and y-axis. The magnetic field generated by each phase conductor can be expressed as:

$$B_A = \frac{\mu_0 I_A}{2\pi r_A} \quad B_B = \frac{\mu_0 I_B}{2\pi r_B} \quad B_C = \frac{\mu_0 I_C}{2\pi r_C} \tag{6}$$

The vector sum of the magnetic field at the sensor is:

$$\begin{aligned}\vec{B} &= B_x i_x + B_y i_y + B_z i_z \\ &= \left[(B_B + B_A\cos\theta + B_C\cos\theta)i_x + (B_A\sin\theta - B_C\sin\theta)i_y\right]\end{aligned} \tag{7}$$

Based on Fig. 2 and (6), the magnetic field on the x and y axes under the overhead line can be expressed as:

$$\begin{bmatrix} B_x \\ B_y \end{bmatrix} = \frac{\mu_0}{2\pi} \begin{bmatrix} \frac{r_{Ay}}{r_A^2} & \frac{r_{By}}{r_B^2} & \frac{r_{Cy}}{r_C^2} \\ \frac{r_{Ax}}{r_A^2} & \frac{r_{Bx}}{r_B^2} & \frac{r_{Cx}}{r_C^2} \end{bmatrix} \begin{bmatrix} I_A \\ I_B \\ I_C \end{bmatrix} \tag{8}$$

where μ_0 is the permeability of air, and its value is $4\pi \times 10^{-7}$ N A^{-2}. The first matrix on the right side of (6) is used as the position matrix, which is determined by the position relationship between the magnetoresistive sensor and the phase conductors. r_A, r_B and r_C are the distances between the three-phase conductors and the sensor, while I_A, I_B and I_C are the three-phase currents, respectively.

After a fault occurs, it can be seen from (1)–(5) and (8) that the current of the healthy phase changes slightly after the fault occurrence, and the currents of the fault phase upstream and downstream of the

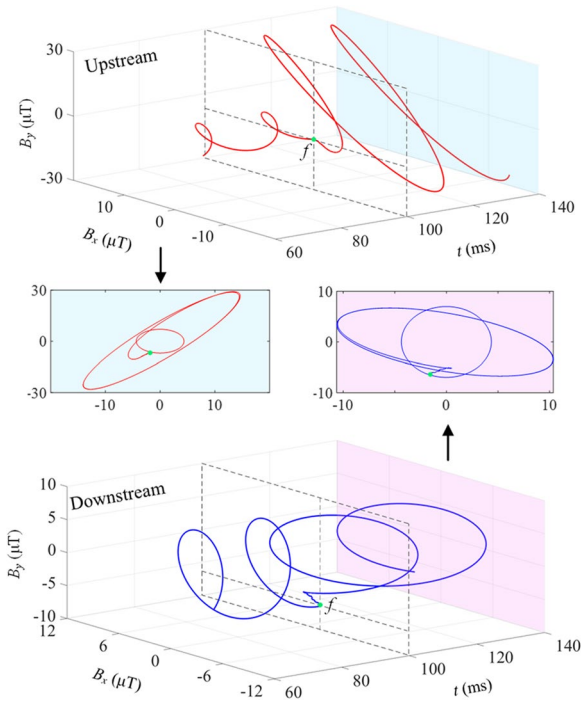

Fig. 3 Dynamic trajectory of magnetic field upstream and downstream of fault point

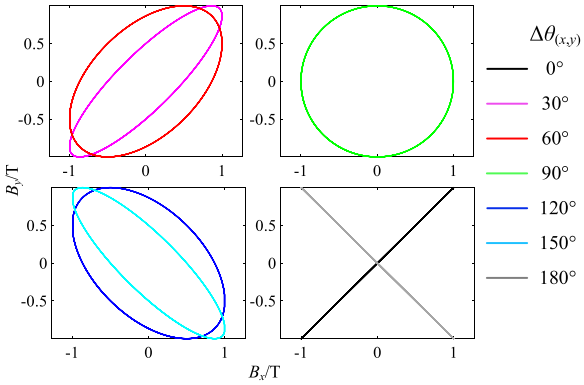

Fig. 4 Lissajous figure with different initial phase angle difference

grounding point are significantly different, resulting in the change of the magnetic field near the overhead line after the fault occurrence. Figure 3 shows the dynamic trajectories of the magnetic fields upstream and downstream of the fault point when a grounding fault occurs for 100 ms.

In Fig. 3, when the dynamic trajectory in the time domain is projected to the plane of the x and y axes, it can be clearly seen that the elliptical structure of the magnetic field trajectory changes significantly after the fault occurrence. At the same time, there are obvious differences in the structure of ellipses upstream and downstream of the fault point. Since the magnetic fields at both ends of the healthy section remain largely the same after the fault, the location criterion can be constructed according to whether there are obvious changes in the structures of the magnetic field ellipses at both ends of the section.

2.2 Least squares method

The least squares method is widely used in line and curve fitting. Its purpose is to find the best matching function of the data. The core idea is to minimize the error between the real value and the predicted value by finding the undetermined coefficients of a set of linear independent functions selected in advance. The error is expressed in the form of square sum. The general form of least squares in an unconstrained optimization problem is given as:

$$\sum_{i=1}^{n} r_i^2 = \sum_{i=1}^{n} \left[y_i - f(x_i, \hat{y}) \right] = \min f(x) \tag{9}$$

where $r_i(x)$, $(i=1, 2,\ldots, n)$ is the residual function, y is the real value and $\hat{y}$ is the predicted value.

In actual distribution networks, the measured magnetic field waveform is a non-standard sine wave because of factors such as the non-periodic component generated by the fault, the error of the monitoring device itself, and external interference, which cannot form Lissajous figures. In this paper, the least squares method is used to fit the dual-axis magnetic field to obtain two standard sine functions, thus forming a Lissajous figure. In the fault location method, the real value is the actual magnetic flux density obtained at each monitoring point, and the predicted value is the function value of the sinusoidal magnetic field wave formed by fitting.

2.3 Lissajous figure

'Lissajous figure' refers to the regular and stable closed curve synthesized by two simple harmonic vibrations with frequencies in a simple integer ratio in the direction perpendicular to each other. In a power system, the Lissajous figure is widely used in two-dimensional syntheses of current, voltage and impedance [29, 30].

For two sine functions x and y with the same frequency:

$$\begin{aligned} x &= B_x = A\sin(\omega t + \theta_1) \\ y &= B_y = B\sin(\omega t + \theta_2) \end{aligned} \tag{10}$$

After transformation, there is:

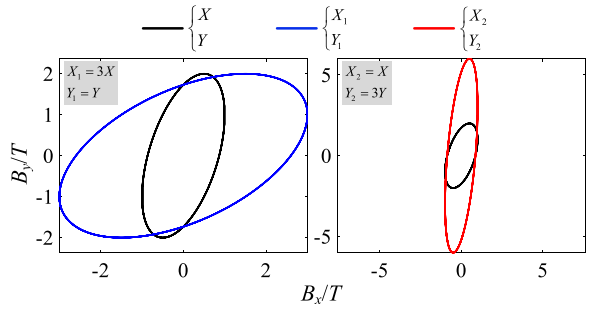

Fig. 5 Lissajous figures at different amplitudes

$$\frac{x^2}{A^2}+\frac{y^2}{B^2}-2\frac{xy}{AB}\cos(\theta_1-\theta_2)-\sin^2(\theta_1-\theta_2)=0 \tag{11}$$

2.3.1 Influence of initial phase angle on Lissajous figure

The difference of the initial phase angle will not affect the period of the synthetic trajectory, but will cause its shape to change. Figure 4 shows the Lissajous figure formed by seven groups of sine functions with amplitude of 1 and same frequency but with different initial phase angle differences ($\Delta\theta=\theta_1-\theta_2$).

It can be seen that the difference $\Delta\theta$ between the initial phase angles of the two sine functions has the same characteristics as the inclination of the major axis of the Lissajous closed figure, such as when $\Delta\theta$ is an acute angle, the inclination of the major axis is also an acute angle, and when $\Delta\theta$ is 90°, the inclination of the major axis is also a right angle. When $\Delta\theta$ is 0° or 180°, the trajectory shrinks to a straight line. Moreover, since the amplitude of each group of functions is 1, the amplitude of the trajectory on each axis is also 1.

The smaller the upstream initial phase angle difference of the fault point, and the larger the downstream initial phase angle difference, the more obvious the difference of the major axis inclination angle of the upstream and downstream Lissajous figures. This means the cosine ratio is more stable to a negative value, i.e., the more likely it is the fault section, and the location results are more reliable.

2.3.2 Influence of amplitude on Lissajous figure

When the amplitude changes, the length–width ratio of the figure will change at the same time. Figure 5 shows a graphic comparison of sine functions with different amplitudes on each axis when each group of functions has the same initial phase angle difference (60°) and frequency ($Y/X=2$).

As shown in Fig. 5, the amplitude of the ellipse on each axis is the same as the amplitude of its corresponding sine function. The length of the major axis of the ellipse increases significantly with the increase of the amplitude of the sine function. For example, when the amplitude of a sine wave moves in the x-axis direction in a group of functions increases by 3 times, the length of its trajectory on the x-axis increases significantly. At the same time, with the increase of the amplitude ratio, the ratio of major to minor axis also increases. In Fig. 5, since $\Delta\theta$ is an acute angle, although the major axis inclination angles change with the change of the function amplitude ratio, they are all acute angles, which is still in accord with the above conclusions.

After the fault occurrence, for the sine function of the dual-axis magnetic field upstream, its amplitude is obviously larger, and the major axis of the synthesized Lissajous figure is also longer, while the axis downstream is shorter because of the small amplitude of the sine function. This can be used as a criterion for location. The greater the amplitude difference between the upstream and downstream sine functions, the greater the difference between the major axes of the two synthesized Lissajous figures, and the more likely the corresponding section is a fault section.

3 Fault location method

The general equation of an ellipse is:

$$ax^2+bxy+cy^2+dx+ey+f=0 \tag{12}$$

Equation (11) derived from Lissajous figure is consistent with the general equation (12) of an ellipse in structure. Therefore, by comparing the two equations, the parameter of the Lissajous figure (i.e. the parameter of the standard sine function) A, B, θ_1, θ_2 can be used to represent the parameter a, b, c, d, e, f of the ellipse equation, as $a=1/A^2$, $b=-2\cos(\theta_1-\theta_2)/AB$, $c=1/B^2$, $d=e=0$, $f=-\sin^2(\theta_1-\theta_2)$.

The geometric center of the ellipse determines its position. The three characteristic quantities of the ellipse's major axis, minor axis and major axis inclination angle can characterize its specific shape. These components can all be represented by ellipse parameters, and the geometric center coordinates are:

$$X=\frac{be-2cd}{4ac-b^2}=0 \qquad Y=\frac{bd-2ae}{4ac-b^2}=0 \tag{13}$$

The expressions of the major axis L, minor axis l and major axis inclination angle δ are:

$$L=\frac{2(aX^2+cY^2+bXY-f)}{a+c-\sqrt{(a-c)^2+b^2}} \tag{14}$$

$$l = \frac{2(aX^2 + cY^2 + bXY - f)}{a + c + \sqrt{(a-c)^2 + b^2}} \tag{15}$$

$$\delta = \frac{1}{2}\arctan\left(\frac{b}{a-c}\right) \tag{16}$$

Since the parameters of the Lissajous figure (i.e. the parameters of the standard sine function) can represent the parameters of the general equation of the ellipse, it can also represent the three characteristic quantities of the ellipse, and the specific expressions are:

$$L = \frac{2\sin^2(\theta_1 - \theta_2)A^2B^2}{A^2 + B^2 - \sqrt{A^4 + B^4 + A^2B^2\left[4\cos^2(\theta_1 - \theta_2) - 2\right]}} \tag{17}$$

$$l = \frac{2\sin^2(\theta_1 - \theta_2)A^2B^2}{A^2 + B^2 + \sqrt{A^4 + B^4 + A^2B^2\left[4\cos^2(\theta_1 - \theta_2) - 2\right]}} \tag{18}$$

$$\delta = \frac{1}{2}\arctan\left(\frac{-2AB\cos(\theta_1 - \theta_2)}{B^2 - A^2}\right) \tag{19}$$

So far, the x and y axes magnetic field data obtained at each monitoring point can be fitted and synthesized to obtain the three characteristic quantities of an ellipse.

It can also be seen from (17) to (19) that the amplitudes and initial phase angles of the magnetic field waveforms on the x-axis and y-axis will affect the three characteristic quantities of the elliptical trajectory. At the same time, when the difference of the phase angle $\theta_1 - \theta_2$ is 0, both L and l are 0. When only the amplitude ratio A/B changes, L/l also changes accordingly. The analysis results meet the conclusions in the principal part above.

The voting method can improve the robustness of the location method, which can be divided into soft voting and hard voting. Hard voting determines the final results according to the principle that the minority obeys the majority, whereas soft voting makes the final judgment through the average probability, which is suitable for predicting the probability of various results. As this paper intends to get a clear and determined fault section, considering the intuitiveness of the results, the hard voting method is adopted.

In this paper, the fault location criterion is constructed by the structural difference of the synthetic trajectory of the dual-axis magnetic field, and the specific location process is shown in Fig. 6.

Major axis criterion: Considering that the difference $L_q - L_h$ between the upstream and downstream major axes of the fault point increases with the increase of

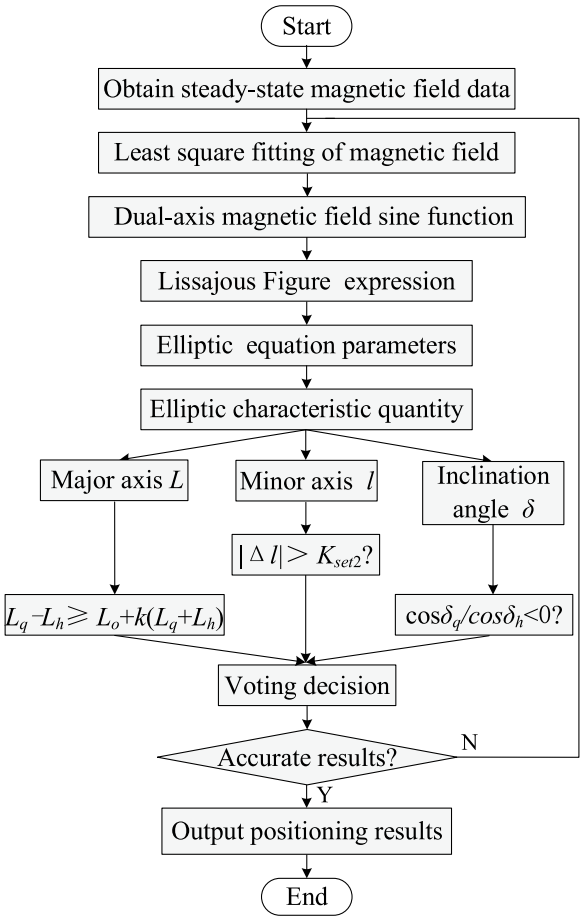

Fig. 6 Fault location flow chart

$L_q + L_h$ of the major axes, the braking amount $L_q + L_h$ is added to form a differential protection with ratio braking characteristics. The action condition is L_q-$L_h \geq L_o + k(L_q + L_h)$, where L_o is the minimum starting length and K is the braking coefficient. The selection of braking coefficient considers the magnetic field error caused by the maximum unbalanced current, which is taken as 0–1, while the minimum starting length takes a small threshold value.

Minor axis criterion: Compare the absolute value $|\Delta l|$ of the difference between the minor axes of the magnetic field ellipses at both ends of each section with the set value K_{set}, and determine the fault section when it is greater than the set value.

Inclination angle criterion: Take the cosine values $\cos\delta_q$ and $\cos\delta_h$ of the inclination angles of the major axes of the magnetic field ellipses at both ends of each section. When the ratio of the cosine values at both ends $\cos\delta_q/\cos\delta_h$ is negative, it is judged as a faulty section, otherwise it is a healthy section.

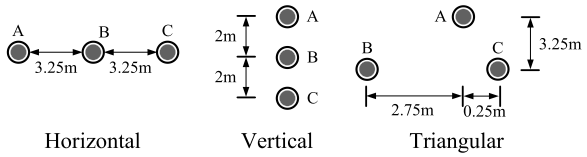

Fig. 7 Different arrangement of three-phase conductors

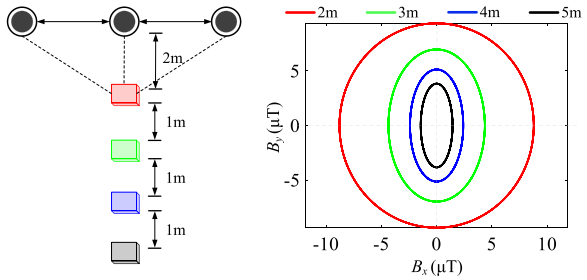

Fig. 8 Magnetic field trajectory at different distances between sensor and lines

4 Influencing factors

4.1 Influence of sensor installation position

The geometric relationship between the installation position of the magnetoresistive sensor on the tower and the three-phase conductors determines the strength of the magnetic field at the sensor, i.e., it affects the shape of the elliptical trajectory.

The three types of tower arrangement commonly used in China are shown in Fig. 7.

In this paper, the horizontal arrangement is taken as an example for analysis. The sensor is installed on the tower, i.e., the horizontal center of the three-phase conductors, and the difference of magnetic field trajectory under different installation heights and its influence on the location algorithm are explored. When the lines and the sensor are very close, although it has a stronger magnetic field its waveform change is not stable and is easily affected by external interference. The sine function obtained by least squares fitting is too different from the actual magnetic field waveform, and consequently, the synthetic Lissajous figure cannot accurately reflect the real line operational situation. When they are far away, the magnetic field is weak, so high sensor precision is required and the effective data may not be monitored, making the location method impossible [31]. Therefore, these two cases are not considered. Figure 8 analyzes the magnetic field elliptical trajectories when the distances between the sensor and the three-phase conductors in the vertical direction are 2 m, 3 m, 4 m, and 5 m, respectively.

No matter how far away the sensor is from the phase conductors, the magnetic field trajectory formed in normal time is a standard ellipse with the major axis on the y-axis. The closer the sensor is to the conductors, the greater the magnetic induction intensity on the x-axis and y-axis, and the longer the major axis and minor axis of the ellipse obtained by the dual-axis, as shown in Fig. 8. At the same time, when the sensor is close to the conductors, the ratio of the major axis to the minor axis is small, close to 1. Therefore, the sensor installed at about 3 m from the horizontal height of the conductors has a better measurement effect.

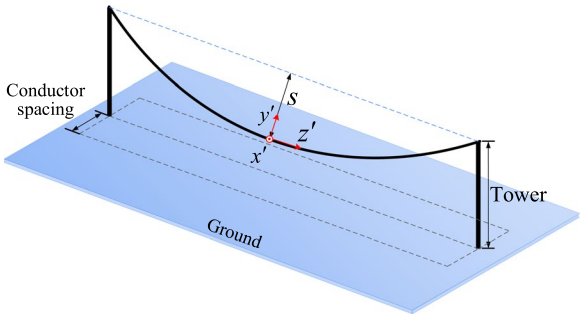

Fig. 9 Actual catenary line

4.2 Influence of conductor sag

The purpose of sag and galloping analysis in this section is to confirm that the magnetic field difference between adjacent monitoring points caused by them is lower than that caused by faults.

In order to simplify the calculation, lines are regarded as horizontal straight conductors, but the actual conductors are catenary lines with sag due to gravity. In real systems, the three phase conductors often have sag of the same height, and the maximum sag point is in the middle of each span.

As shown in Fig. 9, s is the sag. Based on the position of the elementary current on the catenary, a coordinate system is formed, with the lowest point of the intermediate phase conductor as the origin.

Combining the catenary equation and Biot-Savart law, the magnetic flux density at the sensor is [32, 33]:

$$B_{x'} = \frac{\mu_0 I'}{4\pi} \int_{-L_s/2}^{L_s/2} \frac{\sinh(z'/a)(z_s - z') - (y_s - y')}{\left[(x_s - x')^2 + (y_s - y')^2 + (z_s - z')^2\right]^{3/2}} dz' \tag{20}$$

$$B_{y'} = \frac{\mu_0 I'}{4\pi} \int_{-L_s/2}^{L_s/2} \frac{x_s - x'}{\left[(x_s - x')^2 + (y_s - y')^2 + (z_s - z')^2\right]^{3/2}} dz' \tag{21}$$

$$B_{z'} = \frac{\mu_0 I'}{4\pi} \int_{-L_s/2}^{L_s/2} \frac{-\sinh(z'/a)(x_s - x')}{\left[(x_s - x')^2 + (y_s - y')^2 + (z_s - z')^2\right]^{3/2}} dz' \tag{22}$$

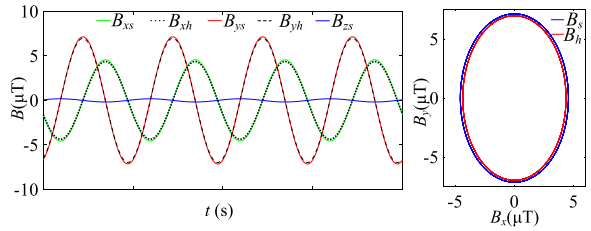

Fig. 10 Magnetic field waveform and synthetic trajectory of each axis

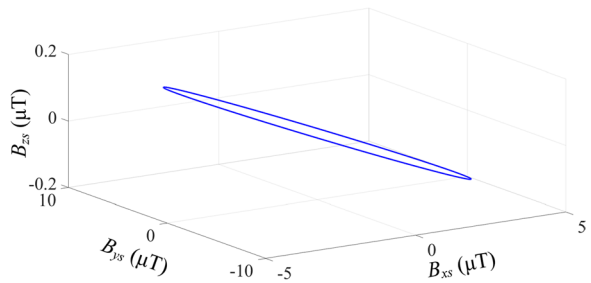

Fig. 11 Magnetic field trajectory in three-dimensional space

where a is the catenary coefficient, I' is the phase current, x_s, y_s and z_s are the sensor coordinates in the x', y' and z' coordinate system, and L_s is the span length.

Taking the horizontally arranged tower as an example, the span L_s is 150 m and the height of the sensor is 3 m below the conductor. When the line is regarded as the ideal situation of the horizontal straight conductor and the catenary with the sag of 1.4 m, the magnetic field waveform and elliptical trajectory are shown in Fig. 10, and the three-dimensional ellipse synthesized in space is shown in Fig. 11. The dual-axis magnetic field and synthetic ellipse of the horizontal straight conductor at the sensor are B_{xh}, B_{yh} and B_h, respectively. When considering sag, the magnetic field on the three axes and dual-axis synthetic ellipse on the three axes are B_{xs}, B_{ys}, B_{zs} and B_s, respectively:

It can be seen from Figs. 10 and 11 that when the conductor sag is 1.4 m, each current element on the conductors is closer to the sensor in the vertical direction, i.e., on the whole, the distance between the conductors and the sensor is smaller. Therefore, compared with the ideal model of horizontal straight line, the magnetic fields of x-axis and y-axis obtained in this case are stronger and the major and minor axes of the synthesized ellipse are longer, but the overall difference is not obvious. At the same time, there is a magnetic field component on the z-axis, but it is very weak, and its amplitude is only 0.1795μT (3.93% of the x-axis amplitude and 2.51% of the y-axis amplitude), which makes it difficult to detect.

Table 1 Errors at different conductor sags

$\|\Delta B\|$ (%)	A phase	B phase	C phase
x-axis	1.85	3.28	1.85
y-axis	2.32	0/0	2.32

0/0 indicates that the magnetic field does not exist in both cases. (When the B phase line is directly above the sensor, the magnetic field on the y-axis is 0.)

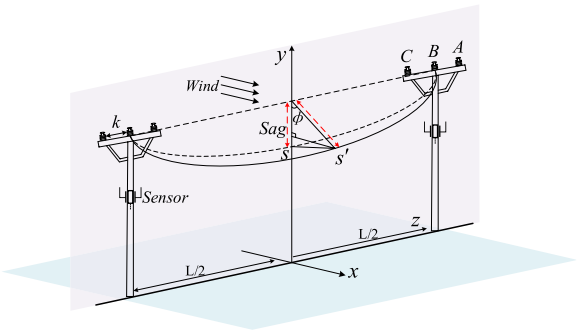

Fig. 12 Galloping line and coordinate axis plane

Therefore, it is not taken as the basis for fault location, and only the magnetic fields on the x-axis and y-axis are considered.

When analyzing the magnetic field difference between the catenary line and horizontal straight conductor, considering that the ratio of magnetic flux density to current is constant. B/I is set at ν, and therefore, $|\Delta B|$ is defined as the error between ν corresponding to different magnetic flux densities. The calculation results are shown in Table 1.

According to the error data in Table 1 and Fig. 10, when considering the influence of sag on the x-axis and y-axis magnetic fields, it is approximately equal to the magnetic field generated by current-carrying straight conductor, and the error is no more than 4%. In addition, it can also be seen from Fig. 10 that the conductor sag does not significantly affect the shape of the magnetic field trajectory. Thus, it can be concluded that the sag can be regarded as having negligible effect on the location method, but the computational complexity will increase if considered. Therefore, in this paper, the influence of sag is ignored.

4.3 Influence of conductor galloping

When the line is galloping because of wind blowing or uneven icing, the line as a whole is approximated as being on a plane, as shown in Fig. 12. As shown, the distance between phase and phase is k, and the line is inclined towards the edge phase (A phase), s and s' are the lowest points of the line when there is no galloping and galloping, respectively.

By analyzing the relationship between each phase conductor and the y–z plane in Fig. 12, the calculation of the basic current coordinate is improved as follows:

Table 2 Magnetic field errors at different angles

$\|\Delta B\|$ (%)	A phase	B phase	C phase
$(O'–O'_{5°})_x$	0.2432	0.0012	0.2246
$(O'–O'_{25°})_x$	1.3664	0.0322	0.9063
$(O'–O'_{50°})_x$	2.9253	0.1227	1.1964
$(O'–O'_{5°})_y$	0.1617	0.0010/0	0.1399
$(O'–O'_{25°})_y$	0.9749	0.0049/0	0.4916
$(O'–O'_{50°})_y$	2.2414	0.0087/0	0.4236

0.0010/0, 0.0049/0, 0.0087/0 indicates that the *v* is 0.0010, 0.0049, 0.0087 at $O'_{5°}$, $O'_{25°}$, $O'_{50°}$ respectively, and is 0 at O'

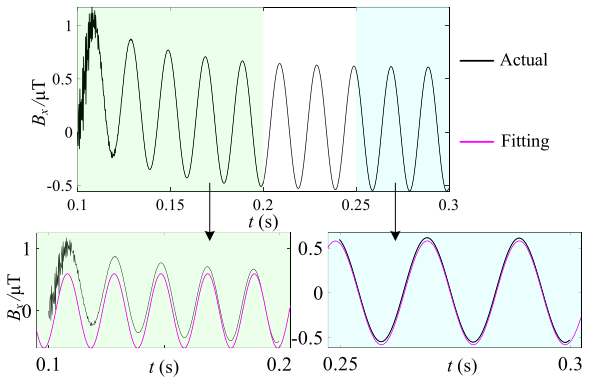

Fig. 13 Fitting effect of B_x under different data windows

$$y' = s - \{s - a[\cosh(z'/a) - 1]\}\cos\varphi \tag{23}$$

$$x' = \{s - a[\cosh(z'/a) - 1]\}\sin\varphi \tag{24}$$

where ϕ is the angle between the plane where the line is located and the y–z plane.

When s is 1.4 m and the line inclination angle ϕ is 5°, 25°, and 50° respectively, the magnetic field errors with current-carrying straight line (the inclination angle of 0°) are shown in Table 2.

It can be seen from Table 2 that the greater the difference between the inclination angles of the two adjacent sections of lines, the higher magnetic field error. However, the overall difference is small, e.g., the error is less than 3% when the inclination angle differs by 50°. Therefore, the magnetic field difference between the two adjacent monitoring points caused by the galloping is far smaller than the magnetic field difference caused by the fault. As the method in this paper is based on the magnetic field difference of adjacent monitoring points to achieve fault location, the small magnetic field difference caused by galloping does not meet the fault criteria and will not cause misjudgment, so it is not considered in the location method.

4.4 Influence of data window

When taking the sampling data window, it is necessary to make the fitted sine function close to the original data and the trajectory close to the standard ellipse. Figure 13 shows the fitting effect of the least squares method on different sampling data windows of B_x after fault, whereas Fig. 14 shows the original waveform of B_y after fault and the trajectory synthesized by B_x and B_y.

From the results in Fig. 13, it can be seen that the transient component at the beginning of the fault has a great impact on the sinusoidal fitting effect. This increases the difference between the fitting function and the original data. This is not conducive to the implementation of the algorithm in this paper, especially with rich transient components. As shown in Figs. 13 and 14, the trajectory synthesized by the original B_x and B_y at the initial stage of the fault has almost no elliptical characteristics.

The two sine functions obtained by the least squares fitting are:

$$\begin{cases} B_{x\_\text{transient}} = 0.5954\sin(310.3t - 0.5721) \\ B_{x\_\text{steady}} = 0.5802\sin(314.5t + 17.56) \end{cases} \tag{25}$$

Similarly, the two y-axis sine functions obtained by least squares fitting are:

$$\begin{cases} B_{y\_\text{transient}} = 1.498\sin(311.3t - 0.5924) \\ B_{y\_\text{steady}} = 1.465\sin(314.4t + 17.73) \end{cases} \tag{26}$$

At the same time, it can be seen from the sine function expressions in (25)–(26) that ω of the function fitted at the initial stage of the fault is often quite different from $2\pi f$ (i.e. = 314), while the value of ω for the function of the stable magnetic field is closer to 314. It can be seen that choosing different data windows will have a great impact on the fitting effect of the least squares method. As the accuracy of the location algorithm can only be guaranteed when it is executed on the real and reliable line operation data, this paper chooses the sine function obtained by the steady-state magnetic field fitting as the premise of location.

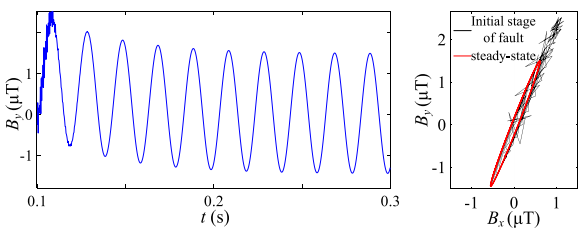

Fig. 14 B_y original waveform and dual-axis synthetic trajectory

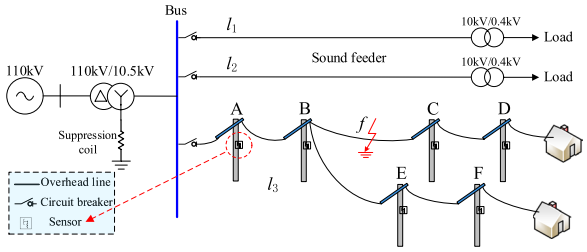

Fig. 15 10 kV distribution network

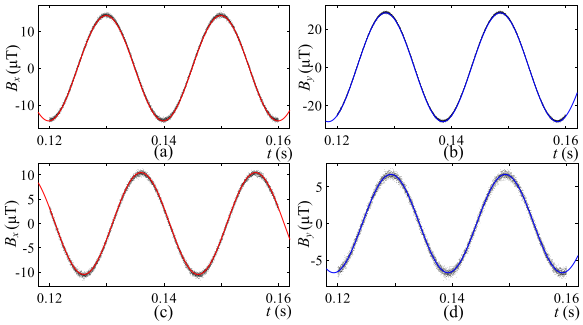

Fig. 16 The fitted sine wave of dual-axis magnetic field. **a** *x*-axis upstream of the fault point; **b** *y*-axis upstream of the fault point; **c** *x*-axis downstream of the fault point; and **d** *y*-axis downstream of the fault point

Table 3 Line parameters

Line type	Phase sequence	R (Ω/km)	L (mH/km)	C (μF/km)
Overhead line	Positive sequence	0.170	1.210	9.700
	Zero sequence	0.230	5.480	6.000

5 Simulation and test verification

PSCAD is used to build a 10 kV distribution network as shown in Fig. 15. The voltage ratio of the system transformer is 110 kV / 10.5 kV, the overcompensation degree of the extinction coil is 5% [34, 35], and the sampling frequency is 20 kHz. A ground fault occurs at *f*, and the line parameters are shown in Table 3:

5.1 Different grounding impedances

The magnetic field data of the second and third cycles after the fault are taken, with added noise at the same time.

When the grounding impedance is 5 Ω, the sine wave of the dual-axis magnetic fields fitted upstream and downstream of the fault point is shown in Fig. 16. It can be seen from Fig. 16 that the high-frequency transient components are already very weak, the waveforms are stable, and the least squares method has a good fitting effect on the scatter data. The expressions of the dual-axis magnetic field functions upstream and downstream of the fault point are:

$$\begin{cases} B_x = 14.29\sin(313.5t - 1.45) \\ B_y = 28.45\sin(313.7t - 1.035) \end{cases} \tag{27}$$

$$\begin{cases} B_x = 10.49\sin(314t + 2.862) \\ B_y = 6.704\sin(314.4t - 1.381) \end{cases} \tag{28}$$

The ellipse general equation parameters are obtained through the sine function parameters and the comparison and derivation above, as shown in Table 4. It can be seen from the parameters in Table 4 that there are obvious differences in the elliptical shapes of the magnetic field upstream and downstream of the fault point.

Based on (27) and (28), the characteristic quantities of the magnetic field trajectory can be obtained, and the characteristic quantities of the upstream and downstream of the fault point under different grounding impedances are simulated, as shown in Table 5, Fig. 17 and Fig. 18.

It can be seen from Figs. 17 and 18 that the magnetic field trajectory is a vertical ellipse in normal conditions. In the case of a fault, with the decrease of grounding impedance, the major axis of the magnetic field ellipse upstream of the fault point increases significantly, while the minor axis only changes slightly. Although the major axis downstream of the fault point also increases, the increase is relatively small. At the same time, comparing Figs. 17 and 18, it can be seen that the inclination angle of the major axis upstream of the fault point gradually decreases from 90° with the decrease of the grounding impedance, while the inclination angle downstream of the fault point gradually increases from 90°. It can be seen from Table 5 that under different grounding impedances, there are obvious differences in the lengths of the major and minor axes at both ends of the fault section. The upstream inclination angle is less than 90° while the downstream inclination angle is greater than 90°. Consequently, the cosine ratio of the two inclination angles is negative, and accurate location results can be obtained. At the same time, the smaller the grounding impedance is, the more obvious the difference between the characteristic quantities of the magnetic field trajectories upstream and downstream of the fault point is. For example, when the grounding impedance is 5 Ω, the difference between the major axis ΔL reaches 40, which is close to twice the length of the downstream major axis. Therefore, this algorithm has high reliability when the

Table 4 Elliptic general equation parameters

Parameter	*a*	*b*	*c*	*d*	*e*	*f*
Upstream	0.0049	−0.0045	0.0012	0	0	−0.1626
Downstream	0.0091	0.0129	0.0223	0	0	−0.7954

Table 5 Characteristic quantity of magnetic field ellipse

Grounding impedance	Location	Major axis	Minor axis	Inclination angle	
				Degrees	Cosine ratio
5Ω	Upstream	62.81	10.44	64.56°	−0.46
	Downstream	22.18	11.31	157.83°	
100Ω	Upstream	18.65	7.89	82.45°	−0.91
	Downstream	14.02	10.10	98.31°	
500Ω	Upstream	14.89	8.47	87.11°	−2.80
	Downstream	13.94	9.02	91.03°	
1000Ω	Upstream	14.41	8.59	88.54°	−1.12
	Downstream	13.95	8.89	91.30°	

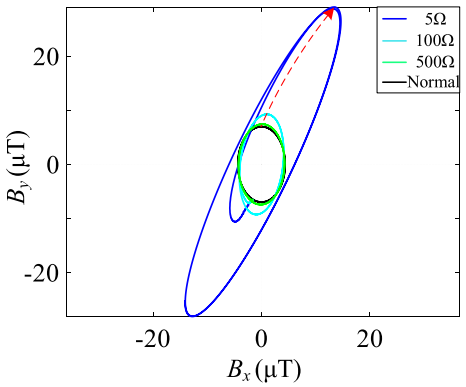

Fig. 17 Magnetic field trajectory upstream of the fault point under different grounding impedances

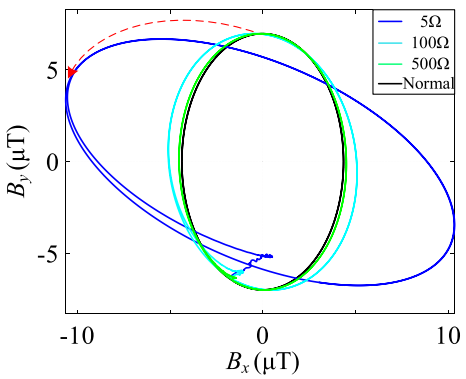

Fig. 18 Magnetic field trajectory downstream of the fault point under different grounding impedances

Table 6 Parameters of magnetic field sine functions under different fault inception angles

Inception angle	Location	Coordinate axis	*A*	*ω*	*θ*
30°	Upstream	*x*	14.29	313.5	−0.93
		y	28.44	313.8	−0.53
	Downstream	*x*	10.49	314.3	−2.94
		y	6.70	314.3	−0.84
60°	Upstream	*x*	14.28	313.8	−0.45
		y	28.45	314.1	−0.05
	Downstream	*x*	10.49	314.6	−2.46
		y	6.71	314.2	−0.30

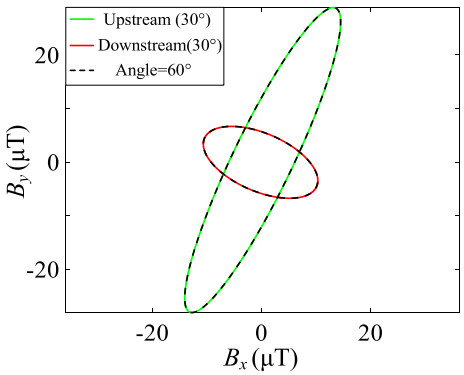

Fig. 19 Ellipses under different fault inception angles

grounding impedance is low, while it also has a certain adaptability to high impedance fault.

5.2 Different fault inception angles

A ground fault occurs in the BC section, and the grounding impedance is also 5 Ω. Considering the influence of different fault inception angles on the elliptical trajectory, with the fault inception angles being 30° and 60°, the parameters of the *x*-axis and *y*-axis sine functions upstream and downstream of the fault point are shown in Table 6, while Fig. 19 shows the magnetic field ellipses under different fault inception angles.

Comparing the parameters of the sine functions when the fault inception angle is 30° and 60° as shown in Table 6, it can be seen that there is basically no difference in the amplitudes of the fitted sine functions under different inception angles. Although the initial phase angles θ of the sine functions are different, the resulting ellipses are almost identical, as shown in Fig. 19. Therefore, it can be concluded that the difference of fault inception angles will only affect the high frequency transient components at the beginning of the fault, while the criterion based on steady-state data will not be affected.

Table 7 Sine Parameters in the case of fault at EF

Fault point	Location	Coordinate axis	*A*	*ω*	*θ*
EF	Upstream	*x*	16.11	313.9	−0.31
		y	26.28	314.1	−0.04
	Downstream	*x*	7.51	314.4	−2.34
		y	4.60	314.2	−0.26

Table 8 Ellipse characteristic quantity of fault at EF

Fault point	Location	Major axis	Minor axis	Inclination angle	
				Degrees	Cosine ratio
EF	Upstream	61.21	7.38	58.92°	−0.56
	Downstream	15.89	7.59	158.15°	

5.3 Different fault location

When the fault occurs in different positions of the line, the change of the upstream and downstream line length of the fault point will lead to a change of the capacitance to the ground of each part, resulting in the difference of current at each position. For this study, the grounding impedance is still set at 5 Ω and the fault inception angle is 60°. When the fault occurs at the end of EF section in Fig. 15 (close to the load side), the sine function parameters of the *x*-axis and *y*-axis magnetic fields upstream and downstream of the fault point and the characteristic quantities of synthetic ellipse are shown in Tables 7 and 8, respectively. In the case of a load side fault, the magnetic field ellipses at both ends of the fault section are shown in Fig. 20.

Comparing Table 6 with Table 7, it can be seen that different fault locations have a great impact on the fitted sine functions, resulting in obvious differences in amplitude. For example, in the case of a fault in the BC section in Table 6, the amplitude difference ΔA of the *x*-axis upstream and downstream of the fault point is only 3.79, whereas for the end of EF section faults in Table 7, ΔA reaches 8.60. The closer the fault is to the load side, the greater the current difference between the upstream and downstream of the fault point is, resulting in greater difference of magnetic field. As shown in Figs. 19, 20 and Table 8, the major and minor axes upstream of the fault point only have small changes, but the major and minor axes downstream of the fault point decrease significantly, resulting in more obvious differences in the characteristic quantities of elliptical trajectories. This is more conducive to the implementation of the location algorithm in this paper.

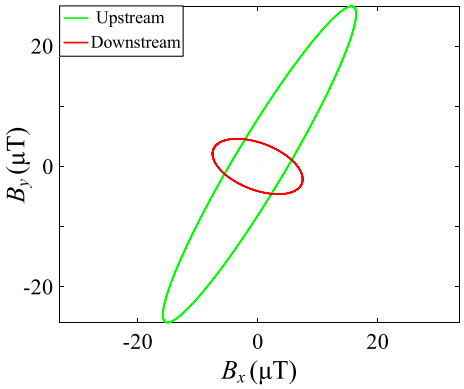

Fig. 20 Magnetic field ellipse in the case of load side fault

6 Comparison with existing methods

For the magnetic field-based location methods, most are based on the amplitude difference and phase difference of the upstream and downstream magnetic fields of the fault point to achieve fault location. With such methods, based on the simulation model in Sect. 5, the absolute value and phase of the magnetic fields upstream and downstream of the fault point are shown in Fig. 21. To verify the reliability of the method, the proposed method is compared with the method in [12], and the results are shown in Table 9.

As seen in Table 9, with the method in [12], the larger the grounding impedance, the smaller the amplitude difference between the upstream and downstream magnetic fields of the fault point. This is not conducive to localization. In addition, the size of the initial phase angle of the fault will also affect the realization of the direction criterion. In contrast, the proposed method contains almost all useful information on the magnetic field under overhead lines, fully reflects the difference between adjacent monitoring points, and has stronger adaptability.

7 Conclusion

By analyzing the difference of elliptical trajectories synthesized by steady-state magnetic fields on the *x*- and *y*-axes after faults, a fault location method based on the characteristics of dual-axis magnetic field trajectories is proposed. In this method, the steady-state magnetic field data on each axis are fitted by the least squares method, and the Lissajous figure is compared with the general elliptic equation to obtain the characteristic quantity expression of the magnetic field trajectory. Finally, the fault section is located through the difference of the characteristic quantities upstream and downstream of the fault point. By analyzing the characteristic quantity of the magnetic field trajectory structure, this method can comprehensively characterize the difference between the upstream and downstream of

Table 9 Localization results of different methods

Method	Criteria	R_f/Ω	SNR/dB	Initial angles	Fault section	Numerical comparisons	√ or ×
Method in [12]	$\Delta f_v > \Delta n_v$	5	–	60°	EF	23.46 > 0	√
		2000	120	0°	BC	0.01 < 1.31	×
	180°-Δf_a < 50°	5	–	60°	EF	40.96° < 50°	√
		2000	120	0°	BC	172.06° > 50°	×
Proposed method	ΔL & $\lvert\Delta I\rvert$ & cosδ	5	–	60°	EF	[45.3,0.2,-0.6]	√
		1000	130	0°	BC	[0.5,0.3,-1,1]	√

Δf_v is the amplitude difference and Δf_a is the direction difference, Δn_v is the amplitude difference of the magnetic fields on both ends of the normal section

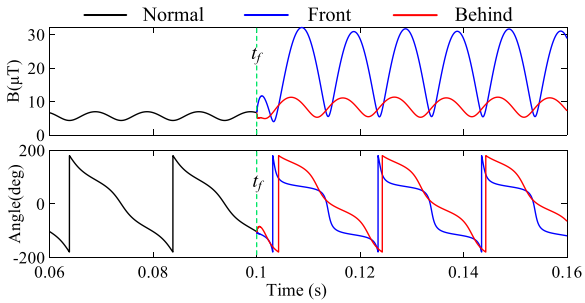

Fig. 21 Absolute value and phase of magnetic fields

the fault point from different aspects, and make the fault location results more reliable and robust.

Acknowledgements
Not applicable.

Author contributions
All authors read and approved the final manuscript.

Funding
This work was supported in part by the National Natural Science Foundation of China (52177114, 61403127) and Jiangxi Electric Power Co., Ltd of State Grid (521820210005, 521820220016).

Availability of data and materials
Not applicable.

Declarations

Competing interests
The authors declare that they have no known competing financial interests or personal relationships that could have appeared to influence the work reported in this paper.

Received: 21 May 2022 Accepted: 3 January 2023
Published online: 30 January 2023

References

1. Gururajapathy, S. S., Mokhlis, H., & Illias, H. A. (2017). Fault location and detection techniques in power distribution systems with distributed generation: a review. *Renewable and Sustainable Energy Reviews, 74*, 949–958.
2. Cheng, L., Wang, T., & Wang, Y. (2022). A novel fault location method for distribution networks with distributed generations based on the time matrix of traveling-waves. *Protection and Control of Modern Power Systems, 7*(4), 698–708.
3. Roostaee, S., Thomas, M. S., & Mehfuz, S. (2017). Experimental studies on impedance based fault location for long transmission lines. *Protection and Control of Modern Power Systems, 2*, 1–9.
4. Aboshady, F. M., Thomas, D. W. P., & Sumner, M. (2019). A new single end wideband impedance based fault location scheme for distribution systems. *Electric Power Systems Research, 173*, 263–270.
5. Trindade, F. C. L., & Freitas, W. (2017). Low voltage zones to support fault location in distribution systems with smart meters. *IEEE Transactions on Smart Grid, 8*(6), 2765–2774.
6. Tian, X., & Shu, H. (2021). A new method of single terminal traveling wave location based on characteristic of superposition of forward traveling wave and backward traveling wave. *International Journal of Electrical Power & Energy Systems, 133*, 107072.
7. Deng, F., Zeng, X., & Pan, L. (2017). Research on multi-terminal traveling wave fault location method in complicated networks based on cloud computing platform. *Protection and Control of Modern Power Systems, 2*, 1–12.
8. Shu, H., Liu, X., & Tian, X. (2021). Single-ended fault location for hybrid feeders based on characteristic distribution of traveling wave along a line. *IEEE Transactions on Power Delivery, 36*(1), 339–350.
9. Dasgupta, A., Nath, S., & Das, A. (2019). Transmission line fault classification and location using wavelet entropy and neural network. *Electric Power Components and Systems, 40*(15), 1676–1689.
10. Jamali, S., Bahmanyar, A., & Ranjbar, S. (2020). Hybrid classifier for fault location in active distribution networks. *Protection and Control of Modern Power Systems, 5*(1), 1–9.
11. Ferreira, K. J., & Emanuel, A. E. (2010). A noninvasive technique for fault detection and location. *IEEE Transactions on Power Delivery, 25*(4), 3024–3034.
12. Huang, Q., Zhen, W., & Pong, P. W. T. (2012). A novel approach for fault location of overhead transmission line with noncontact magnetic-field measurement. *IEEE Transactions on Power Delivery, 27*(3), 1186–1195.
13. Kazim, M., Khawaja, A. H., Zabit, U., & Huang, Q. (2020). Fault detection and localization for overhead 11-kV distribution lines with magnetic measurements. *IEEE Transactions on Instrumentation and Measurement, 69*(5), 2028–2038.
14. Yin, T., Li, J., & Cai, D. (2021). Non-contact fault location and identification method for same-tower multi-circuit transmission lines. *Energy Reports, 7*, 147–158.
15. Neto, J. A. D., Sartori, C. A. F., & Manassero, G. (2021). Fault location in overhead transmission lines based on magnetic signatures and on the extended kalman filter. *IEEE Access, 9*, 15259–15270.
16. Xiao, D., He, T., & Xiao, R. (2020). Segment location for single-phase-to-ground fault in neutral non-effectively grounded system based on distributed electric-field measurement. *Electric Power Systems Research, 184*, 106321.
17. Lekidc, D. M., Mrsic, P. D., Erceg, B. B., Zeljkovic, C. V., Kitic, N. S., & Matic, P. R. (2020). Generalized approach for fault detection in medium voltage distribution networks based on magnetic field measurement. *IEEE Transactions on Power Delivery, 35*(3), 1189–1199.
18. Sifat, A. I., McFadden, F. J. S., Bailey, J., Rayudu, R., & Hunze, A. (2021). Characterization of 400 volt high impedance fault with current and magnetic field measurements. *IEEE Transactions on Power Delivery, 36*(6), 3538–3549.
19. Sarlak, M., & Shahrtash, S. M. (2013). High-impedance faulted branch identification using magnetic-field signature analysis. *IEEE Transactions on Power Delivery, 28*(1), 67–74.
20. Sartori, C. A. F., & Sevegnani, F. X. (2010). Fault classification and detection by wavelet-based magnetic signature recognition. *IEEE Transactions on Magnetics, 46*(8), 2880–2883.
21. Alam, M. R., Muttaqi, K. M., & Saha, T. K. (2020). Classification and localization of fault-initiated voltage sags using 3-D polarization ellipse parameters. *IEEE Transactions on Power Delivery, 35*(4), 1812–1822.
22. Mohanty, R., Sahu, N. K., & Pradhan, A. K. (2021). Time-domain techniques for line protection using three-dimensional cartesian coordinates. *IEEE Transactions on Power Delivery*. https://doi.org/10.1109/TPWRD.2021.3135897

23. Wang, B., Geng, J., & Dong, X. (2018). High-impedance fault detection based on nonlinear voltage–current characteristic profile identification. *IEEE Transactions on Smart Grid, 9*(4), 3783–3791.
24. Wang, B., & Cui, X. (2022). Nonlinear modeling analysis and arc high-impedance faults detection in active distribution networks with neutral grounding via petersen coil. *IEEE Transactions on Smart Grid*. https://doi.org/10.1109/TSG.2022.3147044
25. Gomes, A. D., Costa, M. A., de Faria, T. G. A., & Caminhas, W. M. (2013). Detection and classification of faults in power transmission lines using functional analysis and computational intelligence. *IEEE Transactions on Power Delivery, 28*(3), 1402–1413.
26. Alam, M. R., Muttaqi, K. M., & Bouzerdoum, A. (2015). Characterizing voltage sags and swells using three-phase voltage ellipse parameters. *IEEE Transactions on Industry Applications, 51*(4), 2780–2790.
27. Camarillo-Peñaranda, J. R., & Ramos, G. (2018). Characterization of voltage sags due to faults in radial systems using three-phase voltage ellipse parameters. *IEEE Transactions on Industry Applications, 54*(3), 2032–2040.
28. Camarillo-Peñaranda, J. R., & Ramos, G. (2019). Fault classification and voltage sag parameter computation using voltage ellipses. *IEEE Transactions on Industry Applications, 55*(1), 92–97.
29. D'Angelo, G., Laracca, M., Rampone, S., & Betta, G. (2018). Fast eddy current testing defect classification using Lissajous figures. *IEEE Transactions on Instrumentation and Measurement, 67*(4), 821–830.
30. Gu, L., & Liu, P. (2012). A monitoring method for power condition of AC motors via graphic recognition. *Proceedings of the Chinese Society of Electrical Engineering, 32*(9), 100–108.
31. Grbic, M., Mikulovic, J., & Salamon, D. (2018). Influence of measurement uncertainty of overhead power line conductor heights on electric and magnetic field calculation results. *International Journal of Electrical Power & Energy Systems, 67*, 167–175.
32. Sun, X., Huang, Q., Hou, Y., Jiang, L., & Pong, P. W. T. (2013). Noncontact operation-state monitoring technology based on magnetic-field sensing for overhead high-voltage transmission lines. *IEEE Transactions on Power Delivery, 28*(4), 2145–2153.
33. Khawaja, A. H., Huang, Q., Li, J., & Zhang, Z. (2017). Estimation of current and sag in overhead power transmission lines with optimized magnetic field sensor array placement. *IEEE Transactions on Magnetics, 53*(5), 1–10.
34. Wei, X., et al. (2022). Faulty feeder identification method considering inverter transformer effects in converter dominated distribution network. *IEEE Transactions on Smart Grid*. https://doi.org/10.1109/TSG.2022.3199774
35. Wang, X., Gao, J., Wei, X., Guo, L., Song, G., & Wang, P. (2022). Faulty feeder detection under high impedance faults for resonant grounding distribution systems. *IEEE Transactions on Smart Grid*. https://doi.org/10.1109/TSG.2022.3216731